

X-ray outflows of active galactic nuclei warm absorbers: A 900 ks Chandra simulated spectrum

J.M Ramírez-Velasquez and Javier García

Abstract We report on the performance of the statistical, X-ray absorption lines identification procedure `XLINE-ID`. As illustration, it is used to estimate the time averaged gas density $n_H(r)$ of a representative AGN's warm absorber ($T \approx 10^5$ K) X-ray simulated spectrum. The method relies on three key ingredients: (1) a well established emission continuum level; (2) a robust grid of photoionization models spanning several orders of magnitude in gas density (n_H), plasma column density (N_H), and in ionization states; (3) theoretical curves of growth for a large set of atomic lines. By comparing theoretical and observed equivalent widths of a large set of lines, spanning highly ionized charge states from O, Ne, Mg, Si, S, Ar, and the Fe L-shell and K-shell, we are able to infer the location of the X-ray warm absorber.

1 Introduction

In active galactic nuclei (AGNs), photoionization has been recognized as the main mechanism for the formation of Ultraviolet (UV) and X-ray lines (Bahcall and Kozlovsky (1969)). If the photo-ionized plasma reaches a stable state for their ion populations, they are said to be in photo-ionization equilibrium (PIE). Under the assumption of PIE, one of the principal parameters describing the physical condition of the plasma is the ionization parameter ξ :

J.M Ramírez-Velasquez

Physics Centre, Venezuelan Institute for Scientific Research (IVIC), PO Box 20632, Caracas 1020A, Venezuela - e-mail: josem@ivic.gob.ve and Departamento de Matemáticas, CINVESTAV del I.P.N., 07360 México, D.F., México.

Javier García

Harvard-Smithsonian Center for Astrophysics 60 Garden Street, Cambridge, MA 02138, USA - e-mail: javier@head.cfa.harvard.edu

$$\xi(r) = \frac{L}{n_H(r)r^2}, \quad (1)$$

where L is the ionizing luminosity of the primary source, $n_H(r)$ is the gas density, and r is the distance from the ionizing source to the interacting shell/slab of plasma. Therefore, spectral fitting to the observational data in the X-ray band of a given source combined with a measurement of its luminosity L provide constraints on the degenerated quantity $n_H(r)r^2$. Moreover, in order to have an estimate of the spatial location of the gas absorbing/emitting photons from the primary underlying source, an independent determination of the gas density $n_H(r)$ is required.

Curve of growth (COG) (Spitzer (1998)) is a useful tool to gather information from astrophysical spectra, like ion column density (N_{ion}) using the strength of absorption lines. However, the technique is full of exact requirements and limitations. In order for a line to be used as COG diagnostic tool, firstly (1) a well defined continuum level has to be known prior any construction of the COG. Secondly (2) the synthetic COGs, are usually compared with real measurements of equivalent widths (EWs) of lines. Third (3) the chosen lines must be not saturated respect to the variable we wish to contrast to. Furthermore (4), a reliable *identification* procedure *must be* built on the grounds of a well constructed photoionization modelling (Kallman and Bautista (2001)) which in turn needs a well established set of atomic data. For instance, Badnell (2006) pointed out about the inappropriate use of some dielectronic recombination (DR) rates, which are later discussed by Kallman (2010) in the context of photoionization modelling and the correct use of atomic data (now implemented in the latest version of `xSTAR`) (Bautista and Kallman (2001)).

Following a series of papers related with the computations of K lines of Fe (Palmeri et al. (2002, 2003a)), and K-shell photoabsorption of O ions (Ramírez and Bautista (2002); García et al. (2005, 2011) atomic data (energies, cross sections, lifetimes), Palmeri et al. (2008)) discuss in detail the reliability and accuracy of some sets of these data (medium-Z elements), currently observed in the X-ray spectrum of active galactic nuclei (AGNs, e.g., NGC 3783 Kaspi et al. (2002); Ramírez et al. (2005); Ramírez (2011), MR 2251–178 Ramírez et al. (2008), APM 08279+5255 Ramírez (2008), Ark 564 Ramírez (2013)), in the form of K-absorption lines of H- and He-like Ne, Mg, Si, S, possibly Ar and Ca, and also from lower and medium ionization stages of Si and S (e.g., for MCG-6-30-15 and IRAS 13349+2438) (Holczer et al. (2007)), with the aim of improving the atomic database of the `xSTAR` modelling code.

We report on the accuracy of the statistical method, `xLINE-ID` which allows us to extract time averaged gas density n_H of interacting material surrounding UV+X-rays sources, from EW measurements and *detection* of unsaturated absorption lines respect n_H .

The paper is organized as follows: in the first section, the set of data used, next the details of the method, and finally we delineate the results of the distribution of Doppler velocities found, and compute gas densities. We also discuss the results and conclude. Throughout this paper, we use a cosmology with $H_0 = 70 \text{ km s}^{-1} \text{ Mpc}^{-1}$, $\Omega_M = 0.3$ and $\Omega_\lambda = 0.7$.

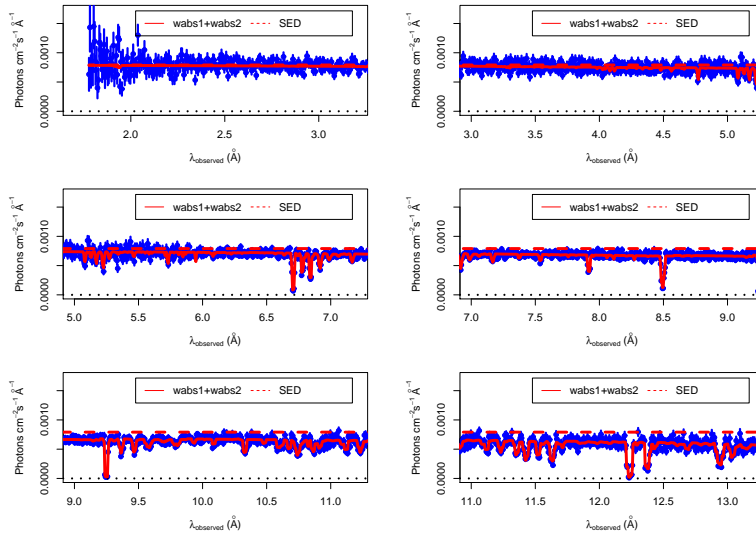


Fig. 1 The continuum emission seen by the material surrounding the UV+X-rays source (1 – 13 Å). Points with error bars are the 900 ks simulated redshifted *Chandra* observation. Solid lines: photoionization model of the absorber (red), and dashed line: the SED.

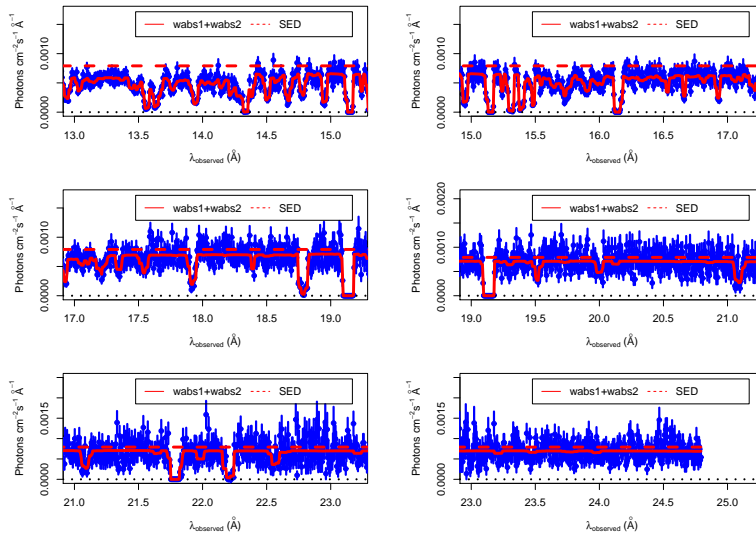


Fig. 2 The continuum emission seen by the material surrounding the UV+X-rays source (13 – 25 Å). Points with error bars are the 900 ks simulated redshifted *Chandra* observation. Solid lines: photoionization model of the absorber (red), and dashed line: the SED.

The set of data and the emission continuum level

One of the main problems in the identification of narrow spectral features in X-ray sources, is the impossibility of contrasting the final atomic identification (ID) of a feature with an input feature, once it has passed through all the instrumentation (effective areas, re-distribution matrix, etc). This is why we aim at assessing this problem, generating a spectrum, over which we have absolute control of every single feature (absorption lines and edges). For that purpose we have created an artificial first dispersion order ± 1 HETG+MEG 900 ks (HETGS with medium energy grating [MEG]), where we know exactly where every feature is located, and described in more detail as follows.

We begin by building a physical model (pow)*wabs1*wabs2 constituted by an UV+X-rays source, redshifted by $z = 0.00976$, emitting a powerlaw (pow), modified by two constant-density ($\log[n_H] = 12$ [cm^{-3}]) absorbers (wabs1, with ionization parameter $\log \xi = 2.08$ [erg cm s^{-1}], column densities $N_H = 10^{22} \text{ cm}^{-2}$, and wabs2, with ionization parameter $\log \xi = 1.15$ [erg cm s^{-1}], column densities $N_H = 10^{21} \text{ cm}^{-2}$)¹. We call this model A. We then use XSPEC 12 to generate a 900 ks MEG spectrum, using appropriate +1 and -1 dispersion orders of MEG effective areas and 1st order response matrix (see science threads in the CIAO main page, <http://cxc.harvard.edu/ciao/>).

Table 1 gives the physical parameters of model A to produce one of the spectra we use in the analysis. Figures (1-2) show: the simulated ± 1 MEG spectrum, (points with error bars); how wabs1 and wabs2 (solid red line) modify the Spectral Energy Distribution (SED)² pow.

Table 1 Physical parameters of model A.

Component	Value	Units
Γ_x	2	–
N^a	0.010	photons $\text{keV}^{-1} \text{cm}^{-2} \text{s}^{-1}$ at 1 keV
z_{pow}	0.00976	–
$\log \xi(1)$	2.08	erg cm s^{-1}
$N_H(1)$	10^{22}	cm^{-2}
$z_{\text{out-wabs1}}$	0.00876	–
$\log \xi(2)$	1.15	erg cm s^{-1}
$N_H(2)$	10^{21}	cm^{-2}
$z_{\text{out-wabs2}}$	0.00836	–

In order to analyze an X-ray spectrum more similar to a real observation (Pérez and Ramírez (2014)), we introduce an outflow velocity to each absorber, $z_{\text{out-wabs1}} = 0.00876$ (300 km s^{-1}) for wabs1, and $z_{\text{out-wabs2}} = 0.00836$ (420 km s^{-1}) to wabs2.

¹ Computed using the code XSTAR and described in more detail in the section **Models: The grid**

² We refer also as the unabsorbed emission continuum from the primary source as seen by the absorber (dashed line in the figures).

Table 2 Physical parameters of model B.

Component	Value	Units
i_{ism}	9.91×10^{20}	cm^{-2}
Γ_x	2	–
N^{a}	0.010	photons $\text{keV}^{-1} \text{cm}^{-2} \text{s}^{-1}$ at 1 keV
z_{pow}	0.00976	–
$\log \xi(1)$	2.08	erg cm s^{-1}
$N_{\text{H}}(1)$	10^{22}	cm^{-2}
$z_{\text{out-wabs1}}$	0.00876	–
$\log \xi(2)$	1.15	erg cm s^{-1}
$N_{\text{H}}(2)$	10^{21}	cm^{-2}
$z_{\text{out-wabs2}}$	0.00836	–

Finally, one additional complication is introduced in model B. We add absorption due to interstellar medium (ism), $i_{\text{ism}} * (\text{pow}) * \text{wabs1} * \text{wabs2}$, so we can study the effect of measuring equivalent widths, with and without consider the unabsorbed continuum emission. Table 2 give parameters for model B. Each case will be carefully analyzed in the next sections.

The `XLINe-ID` method: General Picture

Our goal is to compare measured line equivalent widths (EWs) with synthetic curves generated as functions of the main physical parameters of the system: column density in the line of sight (N_{H}), (log of) ionization parameter ($\log \xi$), and gas density (n_{H}).

The first (1) step to achieve this is to generate a grid of photoionization models (as in AGNs, photoionization is the dominant mechanism for production of spectral lines). Secondly (2), we define the line profile and compute the integrals involved in the EWs of the lines of interest (a list of *detected* features is required as input for `XLINe-ID`). This is a critical step, since none of the main photoionization codes (e.g., `CLOUDY`, `XSTAR`), compute this quantity (by default) for the thousands of lines usually included in the run of the grids, mainly for computational efficiency. The third (3) step is to compare measured EWs with theoretical EWs in order to draw out the parameters of interest.

Models: The grid

Here we describe the building of the grid of models. We use the photoionization code `XSTAR`³ v 2.2 with the most up-to-date atomic database v 2.2.1bn20 (Bautista and Kallman (2001)).

³ <https://heasarc.gsfc.nasa.gov/docs/software/xstar/xstar.html>

The code includes all the relevant atomic processes, including inner shell processes (Palmeri et al. (2003a,b)). It computes the emissivities and optical depths of the most prominent X-ray and UV lines identified in AGN spectra. Our models are based on spherical slabs illuminated by a point-like X-ray continuum source. The input parameters are the source spectrum, the gas composition, the gas density n_H , the column density in the line of sight N_H and the ionization parameter ξ . The source spectrum is described by the spectral luminosity $L_\epsilon = L_{\text{ion}} f_\epsilon$, where L_{ion} is the integrated luminosity from 1 to 1000 Ryd, and $\int_1^{1000 \text{ Ryd}} f_\epsilon d\epsilon = 1$. The spectral function f_ϵ is taken to be a powerlaw $\sim \epsilon^\alpha$ with $\alpha = -1$ (photon index $\Gamma_x = 2$). The gas consists of the following elements, H, He, C, N, O, Ne, Na, Mg, Si, S, Ar, Ca and Fe. We use the abundances of Grevesse et al. (1996) in all our models (and the term *solar* for these abundances). We adopt a turbulent velocity of 200 km s⁻¹. The total ionizing luminosity used is $L_{\text{ion}} = 2.5 \times 10^{44}$ erg s⁻¹.

We have taken two representative ionization parameters: $\log \xi = 2.08$ [erg cm s⁻¹], and $\log \xi = 1.15$ [erg cm s⁻¹]. We call them medium ionization plasma (MIP, represented by wabs1) and low ionization plasma (LIP, represented by wabs2), respectively. Finally due to our interest in testing the sensitivity of the line strengths with the gas density, we run $n_H = 10^{[5,6,7,8,9,10,11,12,13,14,15,16,17,18]}$ cm⁻³, and $N_H = [1,0.1] \times 10^{22}$ cm⁻², for each of the two ionization states, resulting in 28 points in the grid, making it a modest resolution density-COG grid for warm absorber in AGNs.

TRUNK-1: *The identification list model*

We have developed a simple algorithm to identify observed absorption spectral features. The identification is performed by comparing both the line wavelength and optical depth with those computed theoretically in our grid of models. For each model we choose the 500 strongest features, which results in a total of 14,000 theoretical absorption lines ($500 \times 14n_H \times 2N_H$). We shall refer to this as our *identification list*. The simplest way to identify an observed line is to compare its measured wavelength with the theoretical values. However, one must also allow for the possibility of wavelength shifts due to velocity components in the absorbing material. Thus, starting with the best-fit for the line centroid λ_0 of a given observed line, we search for theoretical lines within a $\pm \Delta \lambda_0$ identification window (IW) around λ_0 . This allows for the identification of blue or redshifted lines. If more than one theoretical line is present in the identification window, we choose the line with the largest optical depth at the core (τ_0).

A second observed feature can be found close enough such that its identification window cover a similar range, including the same strong lines. If the next observed feature is identified by the same theoretical line as in the feature just before, we do not allow for repetition but rather choose the second strongest line in the identification window. This allows for the detection of duplets. Nevertheless, this constrain is only applied to two consecutive lines. Thus, if a third consecutive observed line (i.e. two features next) is identify with the same strongest theoretical lines as the

first, this one is assigned again. This allows the detection of more than one velocity component. The result is an identification list based on the strongest predicted absorption line, $\pm\Delta\lambda_0$ Å around a feature detected at λ_0 Å, truncated only *once* for repetition if two features are too close. We call this identification list model TRUNK-1.

Similar studies have been carried out in the past where measured absorption features are compared with a theoretical features in a given identification list (e.g., Krongold et al. (2003); Netzer et al. (2003)). However, these studies present two important limitations: the identification list employed typically contain a relatively small number of theoretical features (e.g., ~ 50), and their identification is based on comparing the wavelength position of the observed feature with those calculated theoretically using undefined identification window (how much is allowed for an observed feature to be compared with theory, e.g., 0.1 Å, is too large). The latter restriction is particularly important because the larger the identification window becomes, the more are the chances of an incorrect identification. To demonstrate the efficacy of our methodology, we have applied the TRUNK-1 algorithm to the synthetic spectra produced with Model A, i.e., the model consisting of two warm absorbers (Table 1).

Because we know exactly which lines are contained in the synthetic spectra, we can then assess how well TRUNK-1 identify the observed lines. Figure 3 shows the level of matching in percent achieved by TRUNK-1. The upper panel in Figure 3 shows the level of matching achieved when the identification is performed solely based on the line position. A good matching is only possible when the identification window is set to the smallest value ($\Delta\lambda_0 = 10^{-4}$ Å). For wider windows the quality of the identification becomes rapidly poor. A much better performance is achieved when, in addition to line positions, line strengths are also compared with the theoretical predictions. This agreement is shown in the lower panel of Figure 3, where is clear that the full TRUNK-1 method is capable to correctly identify no less of 90% of the lines, even for the largest identification window considered ($\Delta\lambda_0 = 0.2$ Å).

The synthetic spectra discussed above contains 239 absorption lines produced with the MIP (wabs 1), and 115 lines produced with the LIP (wabs 2). Although the identification is somewhat better for the lines produced in the absorption component with the smaller redshift (wabs 1), these results indicate that our algorithm can be successfully implemented to real X-ray observations where complex mixture of absorption components can be present. Figure 5 shows the 11–12 Å band of the synthetic spectra, where the known absorption features and those identified by TRUNK-1 are indicated.

Our method correctly identifies 100% of the lines in this band, which we have tested for different widths of the identification window. A similar analysis is performed using a synthetic spectra based on Model B (Table 2), where on top of the two warm absorber components, a third component due to galactic absorption is included (ism). This latter component only includes the continuum (bound-free) photoelectric absorption, thus while it modifies the model continuum it does not introduces any additional absorption features.

In order to illustrate the virtues and caveats of the method we show in Figure 4, six (6) possible cases which are easily solved by it. In panel (a) we have the simplest

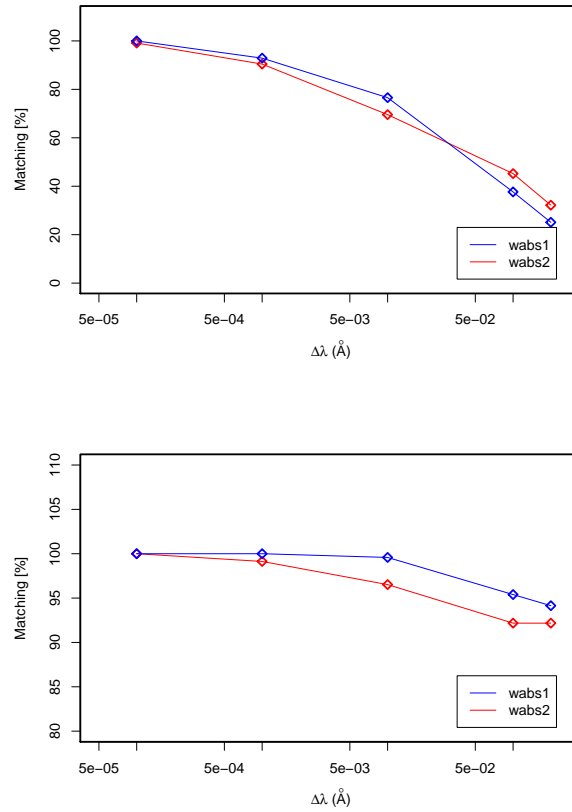


Fig. 3 Top panel: Only first stage of the matching lists process input/TRUNK-1, for the list of the strongest lines coming from our simulation. In the X-axis we open the identification window ($\Delta\lambda$) from 10^{-4} to 0.2 \AA . In blue we present matching process for wabs1, and in red for wabs2. Bottom panel: Second stage of the matching lists process input/TRUNK-1. In the X-axis we open the identification window ($\Delta\lambda$) from 10^{-4} to 0.2 \AA . In blue we present matching process for wabs1, and in red for wabs2 (see Y-axis scale).

possible case. One observed feature $\lambda(O)_1$, has an IW $\Delta\lambda_0$, and only the theoretical line $\lambda(T)_1$ is within the IW. Then $\lambda(O)_1$ is easily identified as $\lambda(T)_1$.

In panel (b), theoretical lines $\lambda(T)_1$ and $\lambda(T)_2$ are within $\Delta\lambda_0$. In this case we simply take the one with the largest optical depth. If we assign τ_1 to $\lambda(T)_1$ and τ_2 to $\lambda(T)_2$ with $\tau_1 > \tau_2$, then $\lambda(O)_1$ is simply identified as $\lambda(T)_1$.

In panel (c) we now have a second observed feature $\lambda(O)_2$. Assuming $\lambda(O)_1$ was already identified as $\lambda(T)_1$ and $\Delta\lambda_{0-2}$ does not contain another theoretical line, $\lambda(O)_2$ will be marked as UNKNOWN. Although this is a rare case, it can be mentioned as a caveat of the algorithm (which also happens with regular ID methods).

In panel (d) a second theoretical line $\lambda(T)_2$ is now in the list of candidates for $\lambda(O)_2$. Assuming $\lambda(O)_1$ was already identified as $\lambda(T)_1$, the TRUNK-1 will force to $\lambda(O)_2$ to be identified as $\lambda(T)_2$ and not as $\lambda(T)_1$, missing the “unlikely” possibility of $\lambda(O)_2$ being a second velocity-component of $\lambda(O)_1$, and by some unknown mechanism $\lambda(T)_2$ was remove from our line-of-sight. Although rare, this also has to be mentioned as a caveat of the method.

In panel (e), we allow the possibility of $\lambda(O)_1$ to have a second velocity-component, if $\lambda(O)_1$ was already identified as $\lambda(T)_1$, and $\lambda(O)_2$ as $\lambda(T)_2$, then $\lambda(O)_3$ will be identified as $\lambda(T)_1$.

And finally in panel (f), there will be two duplets velocity-components with $\lambda(O)_1$ and $\lambda(O)_3$ identified as $\lambda(T)_1$, and $\lambda(O)_2$ and $\lambda(O)_4$ identified as $\lambda(T)_2$.

Although not complete, the list of possible cases cover the situations given in the present work. More cases and/or possibilities can be added to the algorithm in the future, but the results given by Figure 3 (bottom panel), show the method’s performance is at the level of $\approx 90\%$.

In summary we list the limitations of the method:

1. From the beginning, if the photoionization components (e.g., wabs1 and/or wabs2) are not globally fitting the spectrum, the ID process will be dubious.
2. The method expects a list of detected features. If as part of a blend, only one feature is given, the method will ID it as the strongest one, regardless the micro-physics of the blend.
3. The method will not identify a case where the physics changes the ratio $\lambda(T)_1/\lambda(T)_2 > 1$ to < 1 (e.g., case b of Figure 4).
4. Naturally, if the continuum is not well established in the building of the physical model, at the beginning of the process, the absolute measurement of EWs will be wrong (though the comparison between them will be good since they all use the same continuum).
5. The algorithm does not allow the ID of two-velocity component of a feature under the configuration given by case c) of Figure 4. In all those cases visual and manual inspections are required.

Line Profile and EWs

Our procedure receive a list of lines (previously produced in the ID step) and applies the following treads: Each transition produces an absorption optical depth computed with:

$$\tau_\lambda = \tau_0 \phi_\lambda, \quad (2)$$

the optical depth at the core of the line is $\tau_0 = \int_0^{\Delta R} \tau_0(r) dr = N_{\text{ion}}^0 \frac{\pi e^2}{mc} f_{\text{lu}}$, where $\Delta R = N_H/n_H$ is the thickness of the slab, N_{ion}^0 is the column density of the ion at the line core (i.e., $\lambda = \lambda_0$), m is the electron mass, e is the electron charge, c is the speed of light, and f_{lu} is the oscillator strength of the transition. The line profile ϕ_λ ,

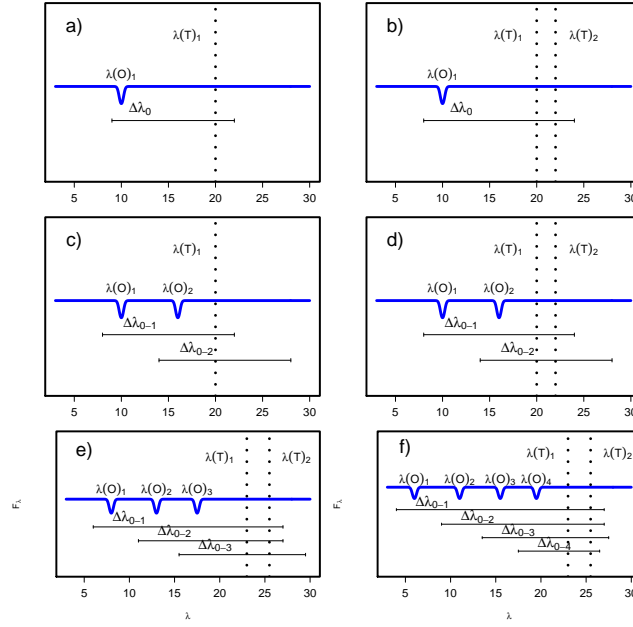


Fig. 4 Complex cases treated by TRUNK-1 for the ID of lines. Panel (a) the simplest case. Panel (b) two candidate lines case. Panel (c) two observed lines have one theoretical line as candidate. Panel (d) two-features, two-candidates (duplets). Panel (e) two velocity-component case. Panel (f) two velocity-component duplets case. See text for details.

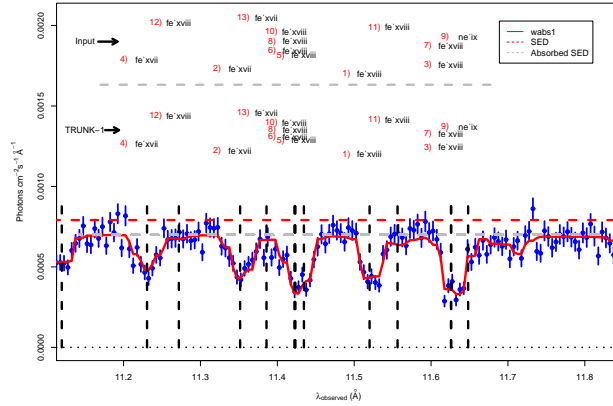


Fig. 5 Simulated spectrum (11-12 Å) showing the input “full-list” given to the procedure TRUNK-1 for wabs1, and the output identification list, using $\Delta\lambda = 10^{-4}$ Å (vertical black dashed lines for wabs1). The absorption lines are enumerated in increasing strength order from 1 to 13.

is assumed to be a Voigt profile (Rybicki and Lightman (1979)). The Doppler broadening parameter $v_{\text{Dop}}^2 = v_{\text{turb}}^2 + v_{\text{therm}}^2$, is the combination of microturbulent (v_{turb}) and thermal broadening (v_{therm}). The last one is computed with $v_{\text{therm}} = \sqrt{\frac{2k_{\text{B}}T}{\mu m_{\text{H}}}}$, where k_{B} is the Boltzmann constant, μm_{H} is the average mass per particle; $\mu \approx 0.6$ for fully ionized solar-metallicity gas. The temperature T is taken from our *XSTAR* calculations. The microturbulent velocity v_{turb} is set to 200 km s^{-1} . Then, we build absorption spectrum for each line (F_{λ} around each feature) and compute EWs:

$$EW = \int 1 - \exp(-\tau_{\lambda}) d\lambda. \quad (3)$$

One important problem we are able to address here, is the difference of measuring absorption line EWs taking into account all the relevant atomic physics, i.e., bound-bound and bound-free transitions, which extend from the SED, in contrast with measurements of EWs made using as the continuum the absorbed SED. We call the first type unabsorbed EWs and the second one absorbed EWs. Figure 6, depicts this problem in a visual manner.

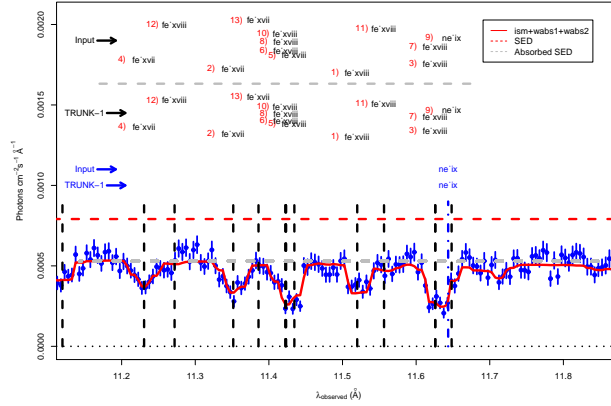


Fig. 6 Simulated spectrum (11-12 Å) showing the input “full-list” given to the procedure trunk-1 for ism+wabs1+wabs2, and the output identification list, using $\Delta\lambda = 10^{-4} \text{ Å}$ (vertical black dashed lines for wabs1, and vertical blue dashed lines for wabs2). The absorption lines are enumerated in increasing order from 1 to 13.

For instance in a model where a single absorber is present (wabs1), we find difference between the level of SED (red dashed line in Figures), and the level of the absorbed SED (gray dashed line), which is the result of the SED’s radiation passing through wabs1. It is clear that measuring EWs using these two different continuum levels will give different results.

Likewise applied to a real observation, the method identifies and present results from H- and He-like ions falling in the X-rays regime, and differences among 6 %

at $\lambda \approx 20 \text{ \AA}$ in lines like Ly_α and Ly_β of OVIII, to 24 % at $\lambda \approx 10 \text{ \AA}$ in lines like MgXI and L-shell of FeXVI-FeXIX, are attributable to the chosen continuum level.

The situation becomes more dramatic as the complexity in absorption increases for model A and model B. We quantify how important this continuum level problem results, where ISM is taking into account. Up to 80 % differences, in both absorbers wabs1 and wabs2, of EW measurements are observed, and it serves as benchmark for comparison of EWs measured using the free-line region (FLR) technique, which make use of absorbed SED as continuum level, as for instance in Kaspi et al. (2002), for measuring line properties of NGC 3783 (see their Table 1).

Results: Deducing distance from the supermassive black hole

In this section we apply our method to the X-ray 900 ks spectrum, introduced in the first section.

Measured vs Theoretical EWs

Theoretical curves of the Ratio= $\frac{\text{EW}_{\text{meas}}}{\text{EW}_{\text{theo}}}$ (measured EW to theoretical EW) vs n_H , for each of the identified features included in the simulation, are compared for wabs1 and wabs2. In Figure 7 (bottom panel) we plot all the Ratios produced through identification of lines (239) using the TRUNK-1 model and the absorber wabs1 ($\log \xi = 2.08$, $N_H = 10^{22} \text{ cm}^{-2}$, $n_H = 10^{12} \text{ cm}^{-3}$). A wavelength-color map has been placed at the right side, so one can read which lines are causing the deviations from 1, that is obtained when $\text{EW}_{\text{meas}} = \text{EW}_{\text{theo}}$. It is natural from this plot to infer what is the spectrum that matches better the observation, i.e., the one with the smaller standard deviation (SD, top axis on the plot) from the mean equal to 1. The same type of graphics has been plotted in Figure 8 for wabs2 ($\log \xi = 1.15$, $N_H = 10^{21} \text{ cm}^{-2}$, $n_H = 10^{12} \text{ cm}^{-3}$), where again we reach the conclusion that the best-fit n_H is the one with smallest SD for Ratio, with mean 1. An analysis of these results will be given in the next section.

COG analysis

In order for a line to be used as density diagnostic, it must be not saturated, and its ratio with measured EWs sensitive respect to n_H . In Figure 8 we present the ratio of measured to theoretical EWs for each of the feature identified and included in building of the spectrum, given by the LIP, with IW, $\Delta\lambda = 10^{-4} \text{ \AA}$. This plot infers that the plasma gas density reproducing best the observation is $n_H = 10^{12} \text{ cm}^{-3}$, where $\text{SD}=0.0$. Fitting procedures allow us to set limits on SD in order to

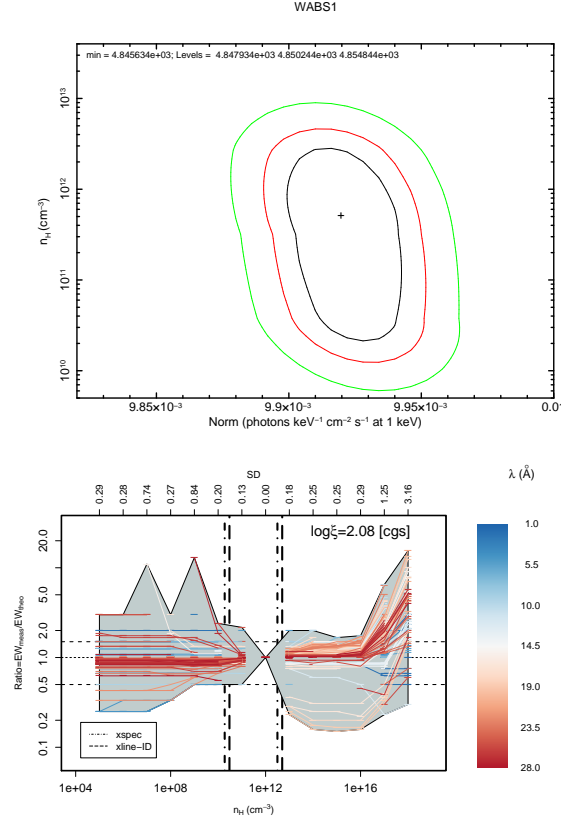


Fig. 7 Top panel: 63 %, 90 % and 95 % 2D confidence level contours on the gas density, n_H , and normalization parameter infer for wabs1. Bottom panel: Ratio= $\frac{EW_{mip}}{EW_{lgo}}$ vs n_H , covering 14 order of magnitudes. At the right side there is a wavelength-color map for the 239 spectral lines detected for the wabs1. Top axis presents the standard deviation (SD) from the mean 1, for each set of lines given by each n_H . Vertical dot-dashed lines are lower- and upper limits computed using spectral fitting within xspec. Vertical dashed lines are lower- and upper limits computed using xline-ID.

achieve confidence level in terms of χ^2 . SD of 0.12-0.15 produce changes > 90 % confidence level on measurements of n_H . We are able to infer the gas density of the spectrum to be $n_H = (2.4 \times 10^{10}, 1.2 \times 10^{13})$ cm⁻³, for the LIP component of the absorbing complex in model B.

The COG ratio shown by the MIP is an excellent case of highly sensitive curve with n_H (see Figure 7). The envolvent (irregular gray polygon) makes a strong constrain of the gas density to be $n_H \approx 10^{12}$ cm⁻³. Again limits on the measurements using SD=0.15-0.17 ($\chi^2 > 2.79$) reports $n_H = (1.9 \times 10^{10}, 3.1 \times 10^{12})$ cm⁻³, for the MIP component of model B.

We checked for the robustness of these measurements with the building of a 2D contours, produced by computing a grid of photoionization models for wabs1 (MIP)

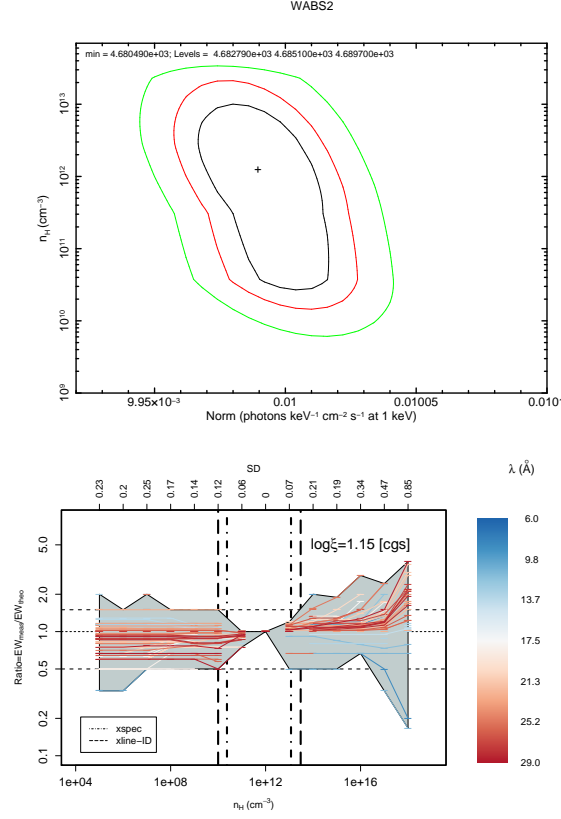


Fig. 8 Top panel: 63 %, 90 % and 95 % 2D confidence level contours on the gas density, n_H , and normalization parameter infer for wabs2. Bottom panel: Ratio= $\frac{EW_{meas}}{EW_{theo}}$ vs n_H , covering 14 order of magnitudes. At the right side there is a wavelength-color map for the 115 spectral lines detected for the wabs2. Top axis presents the standard deviation (SD) from the mean 1, for each set of lines given by each n_H . Vertical dot-dashed lines are lower- and upper limits computed using spectral fitting within xspec. Vertical dashed lines are lower- and upper limits computed using xline-ID.

and wabs2 (LIP), varying $\log(n_H) = 5 - 18$ [cm⁻³], with one point per decade. The result is plotted at the top panel of Figure 7 (for wabs1). From the best-fit $n_H \approx 10^{12}$ cm⁻³, $\chi^2 \approx 4845$ using 4604 PHA bins (and two free parameters), we compute contour level of confidences 63 %, 90 % and 95 % for n_H and the normalization parameter of the powerlaw.

We remark here, that in an independent way, we are obtaining results that are in agreement with the measurements given by our own method. In the bottom panel we compare these xSPEC measurements, i.e., single parameter 90 % confidence level on n_H (vertical dot-dashed line), against the xLINE-ID results. The obvious advantage of our method, is that we can track each of the absorption line which is contributing to the COG ratio density diagnostic, overcoming problems like several χ^2 -minima,

double evaluated best-fit parameter, lack of ability to evaluate what are the spectral ranges contributing to χ^2 , among others.

Velocity density distribution

The second main result of the present analysis can be drawn from Figure 9. There we plot the univariate kernel density estimators (k.d.e) for the Doppler velocity distribution:

$$\hat{f}_{\text{kern}}(v, h) = \frac{1}{nh} \sum_{i=1}^n K\left(\frac{v - V_i}{h}\right), \quad (4)$$

where the kernel function K is a Gaussian and normalized to unity, i.e., $\int K(x)dx = 1$, h is the (constant) bandwidth set to 300 km s^{-1} , and V_1, V_2, \dots, V_n is our random sample of velocities of size n . Each possible identification list has the 500 strongest

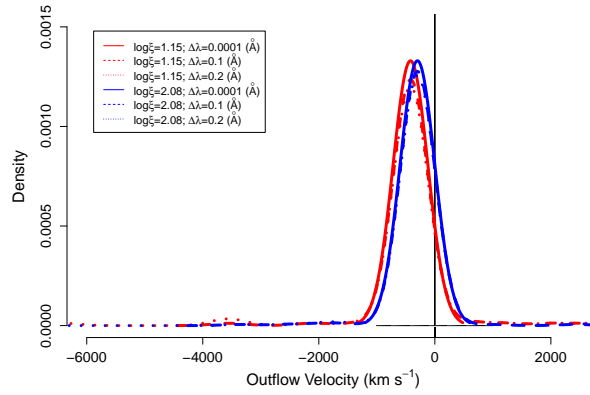


Fig. 9 Probability distribution function (p.d.f) for the flowing velocity of the material absorbing X-rays in the 900 ks *Chandra* simulated spectrum. Solid, dashed and dotted lines are smoothed p.d.fs for the $\Delta\lambda = 10^{-4}, 0.1, 0.2$ respectively. It is used a Gaussian kernel with the best bandwidth of $h = 300 \text{ km s}^{-1}$. Red and blue are LIP and MIP plasmas respectively.

lines for each point of the grid and, as mentioned in section **Models: The grid**, there are 28 grid points. Whenever a detected feature is out of the identification window ($\Delta\lambda \text{ \AA}$ around the feature), is flagged as UNKNOWN and is not taken into account in the probability distribution function (p.d.f) analysis. As we may observe from Fig. 9, one of the main components have peaks at $v_{\text{out}} \approx 300$ (wabs1) and 420 (wabs2) km s^{-1} , confirming the expected result, as this is what we introduce as outflow velocity in our simulated data (see Table 2).

A closer examination also reveals densities different from zero for higher velocity outflows, for instance exhibits by the LIP Si IX $\lambda 6.938 \text{ \AA}$ outflowing at $v_{\text{out}} \simeq 3600 \text{ km s}^{-1}$, and Si VIII $\lambda 7.005 \text{ \AA}$ with $v_{\text{out}} \simeq 3200 \text{ km s}^{-1}$, which are clearly wrong identifications, consequence of the identification window scheme (for the two plasma, solid line has $\Delta\lambda = 10^{-4} \text{ \AA}$, dashed line with $\Delta\lambda = 0.1 \text{ \AA}$, and dotted line with $\Delta\lambda = 0.2 \text{ \AA}$). However we see that the density function of these velocities are very small compared with the components made by right identification.

2 Discussion & Conclusions

In this paper we show how important is to correctly define the level of continuum for EW measurements, which could differ up to $\sim 80 \%$, including or not interstellar absorption. We also show that xLINE-ID is better than 90% in the identification of absorption lines, where more than one absorber is present.

Once we have inferred the gas density from the spectral lines, we can take equation (1) and compute r from it. What is deduced, using the relation $n_H \propto r^{-2}$, and Figure 10, is a suggestion of the MIP located at distances of $r_{MIP} \simeq (0.18 - 1.80) \text{ lt-days}$ ($\log r \simeq 14.7 - 15.7 \text{ [cm]}$), and the LIP located at distances of $r_{LIP} \simeq (0.51 - 5.13) \text{ lt-days}$ ($\log r \simeq 15.1 - 16.1 \text{ [cm]}$). The global picture that emerges from this is that

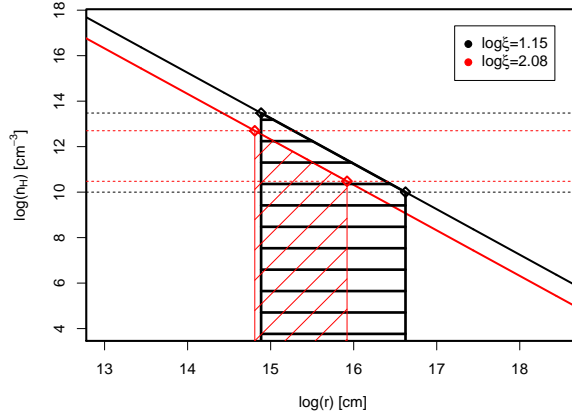


Fig. 10 Spatial location of the absorbers in the analyzed data. The gas density n_H is independently inferred from our COG ratio method. Horizontal lines: MIP (red) and LIP (black). Vertical lines are lower and upper limits on r deduced from equation (1).

highly ($\log \xi \sim 2$) ionized material with gas density ($n_H \sim 10^{12} \text{ cm}^{-3}$) is located closer than the less ionized (colder $\log T \sim 4.7 \text{ K}$) gas. There was no attempt to in-

roduce any pre-established density profile or velocity law in the procedure, and the final relationship between n_H and r was self-consistently achieved.

acknowledgments

This work is partially supported by IVIC project 2013000259. Also, it was partially supported by ABACUS, CONACyT (Mexico) grant EDOMEX-2011-C01-165873.

References

- J. N. Bahcall and B.-Z. Kozlovsky. Some Models for the Emission-Line Region of 3c 48. *Astrophysical Journal*, 158:529, November 1969. doi: 10.1086/150216.
- L. Spitzer. *Physical Processes in the Interstellar Medium*. May 1998.
- T. Kallman and M. Bautista. Photoionization and High-Density Gas. *Astrophysical Journal S.*, 133:221–253, March 2001.
- N. R. Badnell. Dielectronic Recombination of Fe $3p^q$ Ions: A Key Ingredient for Describing X-Ray Absorption in Active Galactic Nuclei. *Astrophysical Journal Letters*, 651:L73–L76, November 2006. doi: 10.1086/509739.
- T. R. Kallman. Modeling of Photoionized Plasmas. *Space Sci. Rev.*, 157:177–191, December 2010. doi: 10.1007/s11214-010-9711-6.
- M. A. Bautista and T. R. Kallman. The XSTAR Atomic Database. *Astrophysical Journal S.*, 134:139–149, May 2001.
- P. Palmeri, C. Mendoza, T. R. Kallman, and M. A. Bautista. On the Structure of the Iron K Edge. *Astrophysical Journal Letters*, 577:L119–L122, October 2002. doi: 10.1086/344243.
- P. Palmeri, C. Mendoza, T. R. Kallman, and M. A. Bautista. A complete set of radiative and Auger rates for K-vacancy states in Fe XVIII–Fe XXV. *A&A*, 403:1175–1184, June 2003a. doi: 10.1051/0004-6361:20030405.
- J. M. Ramírez and M. A. Bautista. Resolving resonances in R-matrix calculations. *Journal of Physics B Atomic Molecular Physics*, 35:4139–4146, October 2002. doi: 10.1088/0953-4075/35/20/302.
- J. García, C. Mendoza, M. A. Bautista, T. W. Gorczyca, T. R. Kallman, and P. Palmeri. K-Shell Photoabsorption of Oxygen Ions. *Astrophysical Journal S.*, 158:68–79, May 2005. doi: 10.1086/428712.
- J. García, J. M. Ramírez, T. R. Kallman, M. Witthoef, M. A. Bautista, C. Mendoza, P. Palmeri, and P. Quinet. Modeling the Oxygen K Absorption in the Interstellar Medium: An XMM-Newton View of Sco X-1. *Astrophysical Journal Letters*, 731:L15, April 2011. doi: 10.1088/2041-8205/731/1/L15.
- P. Palmeri, P. Quinet, C. Mendoza, M. A. Bautista, J. García, and T. R. Kallman. Radiative and Auger Decay of K-Vacancy Levels in the Ne, Mg, Si, S, Ar, and Ca Isonuclear Sequences. *Astrophysical Journal S.*, 177:408–416, July 2008. doi: 10.1086/587804.
- S. Kaspi, W. N. Brandt, I. M. George, H. Netzer, D. M. Crenshaw, J. R. Gabel, F. W. Hamann, M. E. Kaiser, A. Koratkar, S. B. Kraemer, G. A. Kriss, S. Mathur, R. F.

- Mushotzky, K. Nandra, B. M. Peterson, J. C. Shields, T. J. Turner, and W. Zheng. The Ionized Gas and Nuclear Environment in NGC 3783. I. Time-averaged 900 Kilosecond Chandra Grating Spectroscopy. *Astrophysical Journal*, 574:643–662, August 2002.
- J. M. Ramírez, M. Bautista, and T. Kallman. Line Asymmetry in the Seyfert Galaxy NGC 3783. *Astrophysical Journal*, 627:166–176, July 2005. doi: 10.1086/430202.
- J. M. Ramírez. Kinematics from spectral lines for AGN outflows based on time-independent radiation-driven wind theory. *Rev. Mexicana Astron. Astrofis.*, 47: 385–399, October 2011.
- J. M. Ramírez, S. Komossa, V. Burwitz, and S. Mathur. Chandra LETGS Spectroscopy of the Quasar MR 2251-178 and Its Warm Absorber. *Astrophysical Journal*, 681:965–981, July 2008. doi: 10.1086/587949.
- J. M. Ramírez. Physical and kinematical properties of the X-ray absorber in the broad absorption line quasar APM 08279+5255. *A&A*, 489:57–68, October 2008. doi: 10.1051/0004-6361:200810264.
- J. M. Ramírez. Chandra LETGS observation of the variable NLS1 galaxy Ark 564. *A&A*, 551:A95, March 2013. doi: 10.1051/0004-6361/201220424.
- T. Holczer, E. Behar, and S. Kaspi. Absorption Measure Distribution of the Outflow in IRAS 13349+2438: Direct Observation of Thermal Instability? *Astrophysical Journal*, 663:799–807, July 2007. doi: 10.1086/518416.
- L. F. Pérez and J. M. Ramírez. *Statistical Methods for the Detection of Flows in Active Galactic Nuclei Using X-Ray Spectral Lines*. Computational and Experimental Fluid Mechanics with Applications to Physics, Engineering and the Environment. / Leonardo Sigalotti (Editor), Jaime Klapp (Editor), Eloy Sira (Editor) : Springer International AG, 2014, pp 521, 2014.
- P. Palmeri, C. Mendoza, T. R. Kallman, M. A. Bautista, and M. Meléndez. Modeling of iron K lines: Radiative and Auger decay data for Fe II-Fe IX. *A&A*, 410:359–364, October 2003b. doi: 10.1051/0004-6361:20031262.
- N. Grevesse, A. Noels, and A. J. Sauval. Standard Abundances. In *Astronomical Society of the Pacific Conference Series*, page 117, 1996.
- Y. Krongold, F. Nicastro, N. S. Brickhouse, M. Elvis, D. A. Liedahl, and S. Mathur. Toward a Self-Consistent Model of the Ionized Absorber in NGC 3783. *Astrophysical Journal*, 597:832–850, November 2003.
- H. Netzer, S. Kaspi, E. Behar, W. N. Brandt, D. Chelouche, I. M. George, D. M. Crenshaw, J. R. Gabel, F. W. Hamann, S. B. Kraemer, G. A. Kriss, K. Nandra, B. M. Peterson, J. C. Shields, and T. J. Turner. The Ionized Gas and Nuclear Environment in NGC 3783. IV. Variability and Modeling of the 900 Kilosecond Chandra Spectrum. *Astrophysical Journal*, 599:933–948, December 2003. doi: 10.1086/379508.
- G. B. Rybicki and A. P. Lightman. *Radiative processes in astrophysics*. 1979.